Position Regulation of a Conductive Nonmagnetic Object With Two Stationary Rotating-Magnetic-Dipole Field Sources

Devin K. Dalton, *Member, IEEE*, Griffin F. Tabor, *Member, IEEE*, Tucker Hermans, *Senior Member, IEEE*, and Jake J. Abbott, *Senior Member, IEEE*

***Abstract*—Eddy currents induced by rotating magnetic dipole fields can produce forces and torques that enable dexterous manipulation of conductive nonmagnetic objects. This paradigm shows promise for application in the remediation of space debris. The induced force from each rotating-magnetic-dipole field source always includes a repulsive component, suggesting that the object should be surrounded by field sources to some degree to ensure the object does not leave the dexterous workspace during manipulation. In this article, we show that it is possible to fully control the position of an object in a workspace near the midpoint between just two stationary field sources. A given position controller requires a low-level force controller. We propose two new force controllers, and compare them with the state-of-the-art method from the literature. One of the new force controllers is particularly good at not inducing parasitic torques, which is hypothesized to be beneficial for future tasks manipulating and detumbling rotating resident space objects. We perform experimental verification using numerical and physical simulators of microgravity.**

***Index Terms*—Manipulation planning, motion control, space robotics and automation.**

I. Introduction

SIX-DEGREE-OF-FREEDOM (6-DOF) manipulation of electrically conductive, nonmagnetic objects made of materials such as aluminum is possible using multiple static magnetic field sources generating rotating dipole fields with controllable speeds about controllable axes [1]. Such magnetic field sources can be omnidirectional electromagnets or robot-positioned rotating permanent magnets [2]. The method works by using dynamic magnetic fields to induce eddy currents in an object, which in turn interact with the applied magnetic field and induce forces and torques on the object. We focused our force–torque modeling and initial manipulation experiments on conductive spheres [1], which we hypothesized could serve as first-order approximations for other objects. We then actively adapted the radius and conductivity of the spherical model based on the observed object motion to enable manipulation of unknown and nonspherical objects [3]. We found that each field source always generates a repulsive force component, regardless of any other force and torque components, with the result being that position control of an object requires at least two field sources [1]. In our most recent contribution on this topic, we showed that two or more fields sources working together in a purely open-loop fashion can pull an object, from a limited set of initial conditions, into the central workspace between the field sources [4].

We are primarily interested in applications of this phenomenon in the microgravity environment of space, for which eddy-current-based actuation has received substantial attention in recent years. The motivation for eddy-current-based actuation is the reduction of the chance of destructive collision, compared to traditional contact-based methods, with engineered space objects that contain large quantities of aluminum [5]. Importantly, the relatively weak induced forces and torques of the eddy currents are potentially sufficient in microgravity, as they need not overcome the object's weight or other disturbances. The induced accelerations may be small, but long time scales may be acceptable for certain applications in space. Prior work in eddy-current-based actuation for space applications has largely considered detumbling of objects using static magnetic fields [6], [7], [8], [9] or rotating Halbach arrays [10], [11]. This work has been motivated by the remediation of space debris, which is a major problem facing humanity [12], [13]; this is our primary motivation as well. Other prior work in eddy-current-based actuation has considered the use of rotating magnets [14], rotating Halbach arrays [15], or electromagnets [16] housed within a robotic spacecraft to enable it to traverse the exterior of

Received 8 April 2024; accepted 23 July 2024. Date of publication 4 September 2024; date of current version 11 October 2024. This work was supported in part by the Air Force Research Laboratory, Aerospace Systems Directorate, Rocket Propulsion Division, in part by the AFWERX, AFRL/RGKB under Contract FA9453-22-C-A044, and in part by the National Science Foundation under Grant 2149585. This article was recommended for publication by Associate Editor Gionata Salvietti and Editor Timothy Bretl upon evaluation of the reviewers' comments. *(Corresponding author: Jake J. Abbott.)*

Devin K. Dalton is with the University of Utah Robotics Center and Department of Mechanical Engineering, Salt Lake City, UT 84112 USA, and with the United States Air Force, Air Force Nuclear Weapons Center, Albuquerque, NM 87117 USA, and also with Engineering Liaison Office, 66877 Ramstein, Germany (e-mail: devin.dalton@us.af.mil).

Griffin F. Tabor is with the University of Utah Robotics Center and Kahlert School of Computing, Salt Lake City, UT 84112 USA (e-mail: griffin.tabor@utah.edu).

Tucker Hermans is with the University of Utah Robotics Center and Kahlert School of Computing, Salt Lake City, UT 84112 USA, and also with NVIDIA, Seattle, WA 98052 USA (e-mail: tucker.hermans@utah.edu).

Jake J. Abbott is with the University of Utah Robotics Center and Department of Mechanical Engineering, Salt Lake City, UT 84112 USA (e-mail: jake.abbott@utah.edu).

This article has supplementary downloadable material available at https://doi.org/10.1109/TRO.2024.3454568, provided by the authors.

Digital Object Identifier 10.1109/TRO.2024.3454568

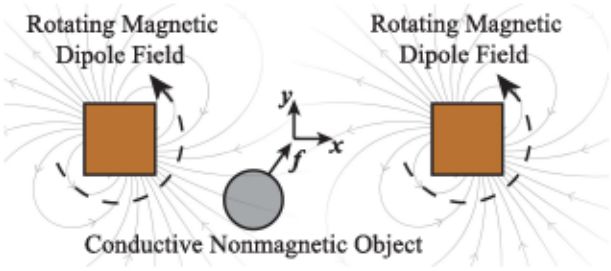

Fig. 1. Schematic depicting two stationary rotating-magnetic-dipole field sources that create eddy-current-induced forces on a conductive nonmagnetic object to control its position.

a larger conductive nonmagnetic structure, such as the International Space Station.

A two-armed robot equipped with magnetic end-effectors [6] could rendezvous with an object [17] and place the two end-effectors on opposite sides of the object to manipulate it. In this article, we are particularly interested in position regulation of an object to the midpoint between the two field sources, to be detumbled by a secondary method that applies torque counter to the angular velocity of the object but which will also induce destabilizing forces; this secondary method could use our same rotating-magnetic-dipole field sources or it could use one of the other technologies that have been proposed for detumbling. For such an application, it may be desirable to induce the smallest parasitic torque possible during the position-regulation phase, so as to not perturb the axis of rotation of the object. However, our previous closed-loop position controllers solve a greedy optimization problem to find the single field source that instantaneously minimizes the error between the desired and induced force–torque wrench [1], [3], with the assumption that other field sources can correct for errors in future control cycles; the accuracy of this assumption is reduced as the number of field sources is reduced to just two.

In this article, we implement a basic three-degree-of-freedom (3-DOF) position controller, nominally at the midpoint between two field sources (see Fig. 1). This requires a low-level 3-DOF force controller, for which we present two: one minimizes parasitic applied torque, but often has an artificially low saturation on force magnitude; the other can often achieve higher force magnitudes, or can achieve a given force more efficiently, but may also induce parasitic torques. Our analytical developments explicitly consider spherical objects, as in [1], [3], and [4]. In numerical and experimental simulations of microgravity, we show that it is, in fact, always possible to perform 3-DOF position control using just two stationary field sources, provided the object is in a nominal workspace near the midpoint between the two field sources. We compare the two new force controllers with each other and with the state-of-the-art controller from [3] (which is an improvement over the controller in [1]).

II. Review of the Force–Torque Model

We begin by summarizing our model of induced force–torque on a solid spherical conductive object due to a rotating magnetic dipole field. It begins with the model from [1], which considered the object in three canonical positions relative to the rotating dipole. It then incorporates the extension of [3], which considered other locations of the object with respect to the rotating dipole, using spherical coordinates (see Fig. 2). The magnetic dipole can be abstracted as a point dipole $\boldsymbol{m}$ at position $\mathscr{P}_m$, rotating with angular velocity $\boldsymbol{\omega}$, such that $\boldsymbol{m}$ is orthogonal to $\boldsymbol{\omega}$. We can describe the position of the center of the conductive object as $\mathscr{P}_o$ and construct a relative displacement vector $\boldsymbol{\rho} = \mathscr{P}_o - \mathscr{P}_m$. The relative position of the conductive object is described by three coordinates with respect to the rotating magnetic dipole: a distance $\rho = \|\boldsymbol{\rho}\|$, a polar angle θ measured from the dipole's rotation vector $\boldsymbol{\omega}$, and an azimuthal angle ϕ measuring a right-handed rotation about $\boldsymbol{\omega}$. In this coordinate system, the three canonical positions are described by $\theta = 0°$, $\theta = 90°$, and $\theta = 180°$.

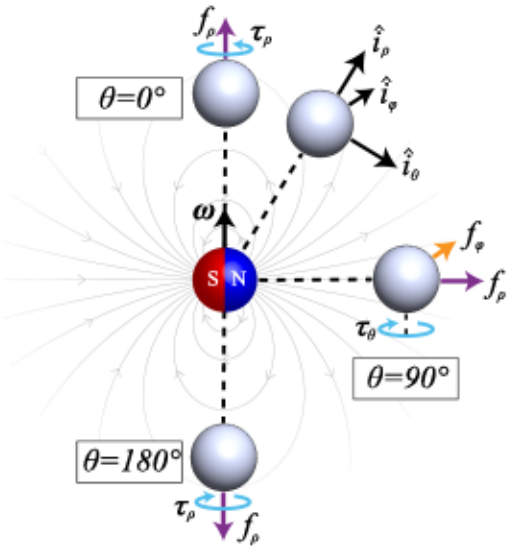

Fig. 2. Eddy-current-induced forces and torques shown in a spherical coordinate system to describe arbitrary positions of a conductive nonmagnetic object relative to a rotating magnetic dipole (with the dipole field depicted at a given instant). The orthonormal basis vectors at a given location are defined as shown, with $\hat{\boldsymbol{\imath}}_\phi = \hat{\boldsymbol{\imath}}_\rho \times \hat{\boldsymbol{\imath}}_\theta$. The three canonical positions in [1], and their respective forces and torques, are recast in the spherical coordinate system as in [3]. The arrowhead on τ_ρ at $\theta = 180°$ depicts the positive sign convention, which is opposite to the actual torque direction for the $\boldsymbol{\omega}$ shown. All other force/torque arrowheads depict both the positive sign convention and the actual force/torque direction for the $\boldsymbol{\omega}$ shown. In this image, $\hat{\boldsymbol{\imath}}_\phi$ and $\boldsymbol{f}_\phi$ point into the page.

The steady-state time-averaged eddy-current-induced force $\boldsymbol{f}$ and torque $\boldsymbol{\tau}$ were modeled parametrically, at the three canonical positions, as a function of the electrical conductivity σ of the sphere, the distance ρ from the dipole (modeled as a point, which would be at the center of a physical source) to the center of the sphere, the radius r of the conductive sphere, the magnetic dipole strength $m = \|\boldsymbol{m}\|$, the dipole rotation frequency $\omega = \|\boldsymbol{\omega}\|$, and the permeability of the environment μ. Using the Buckingham Π theorem, we found that each of the forces and torques could be characterized using just two independent dimensionless Π groups (see Table I). The resulting model took the form

$$f, \tau = \frac{\mu_0 m^2 \left(c_0 \sigma \mu_0 \omega r^2\right)^{c_1 \left(\sigma \mu_0 \omega r^2\right)^{c_2}} 10^{c_3}}{\left(\frac{\rho}{r}\right)^{c_4} r^{c_5}} \tag{1}$$

TABLE I
INDUCED FORCE AND TORQUE, AND THE SIX INDEPENDENT PARAMETERS THAT AFFECT THEM, ADAPTED FROM [1]

Parameter	Units	Π group
f	N	$\Pi_0 = fr^4\mu^{-1}m^{-2}$
τ	N·m	$\Pi_0 = \tau r^3\mu^{-1}m^{-2}$
σ	$A^2{\cdot}s{\cdot}N^{-1}{\cdot}\ m^{-2}$ ($S{\cdot}m^{-1}$)	$\Pi_1 = \sigma\mu\omega r^2$
ρ	m	$\Pi_2 = \rho r^{-1}$
r	m	
m	$A{\cdot}m^2$	
ω	s^{-1} (Hz)	
μ	$N{\cdot}A^{-2}$	

TABLE II
COEFFICIENTS FOR THE MODELS IN (1) FOR TWO CANONICAL POSITIONS, BASED ON FINITE-ELEMENT-ANALYSIS (FEA) SIMULATIONS AND EXPERIMENTS [1], RECAST IN SPHERICAL COORDINATES [3]

FEA simulations							
θ	$f,\ \tau$	Coefficients					
		c_0	c_1	c_2	c_3	c_4	c_5
0°	f_ρ	430	2.95	−0.101	−9.26	7	4
0°	τ_ρ	6840	3.00	−0.0986	−13.2	6	3
90°	f_ρ	266	2.60	−0.101	−7.65	7	4
90°	f_ϕ	6040	3.45	−0.102	−14.3	7	4
90°	τ_θ	8100	3.60	−0.0985	−15.7	6	3
Experimental							
θ	$f,\ \tau$	Coefficients					
		c_0	c_1	c_2	c_3	c_4	c_5
0°	f_ρ	467	2.81	−0.0969	−9.75	7	4
0°	τ_ρ	6900	3.35	−0.0990	−14.9	6	3
90°	f_ρ	282	3.20	−0.0980	−9.41	7	4
90°	f_ϕ	5870	3.49	−0.0973	−14.6	7	4
90°	τ_θ	8000	3.40	−0.0928	−15.0	6	3

for each of the force and torque components, where $\mu_0 = 4\pi \times 10^{-7}\ \mathrm{N \cdot A^{-2}}$ is the permeability of free space (μ_0 is the only value of μ of any practical interest). The coefficients for the $\theta = 0°$ and $\theta = 90°$ positions—which is all that we will need going forward, due to the symmetry of $\theta = 0°$ and $\theta = 180°$—are provided in Table II. The model (1) is a far-field model, which may underpredict the magnitude of force and torque when $\rho < 1.5r$, approximately. The model was also developed using data in the range $0 \leq \Pi_1 \leq 20$, so extrapolation beyond this range should be done with caution.

Given the force and torque values at $\theta = 0°$ and $\theta = 90°$, we are able to construct the force and torque at other values of θ using a set of simple trigonometric functions, which embody the type of symmetries that we might expect. The equations that describe the force and torque components in spherical coordinates—at arbitrary values of ρ and θ, and not requiring ϕ due to symmetry—which call the canonical-position model (1), are as follows:

$$f_\rho(\rho,\theta) = \left(\frac{f_\rho(\rho,90°) + f_\rho(\rho,0°)}{2}\right) - \left(\frac{f_\rho(\rho,90°) - f_\rho(\rho,0°)}{2}\right)\cos(2\theta) \quad (2)$$

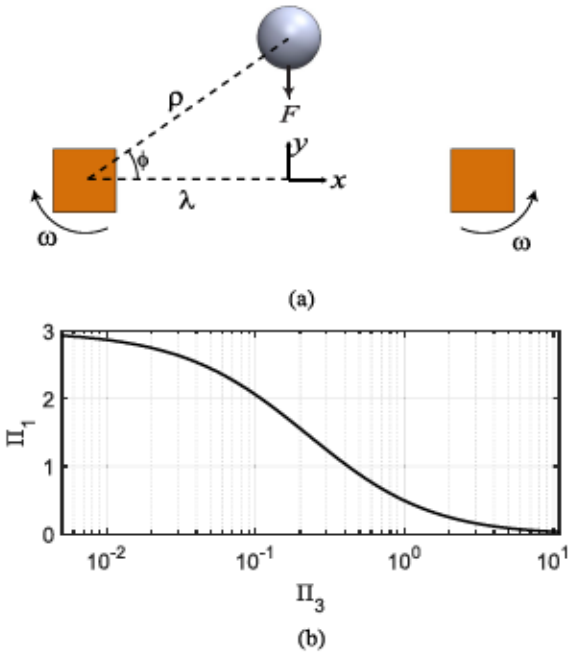

Fig. 3. Optimal attraction along axis of symmetry of two duty-cycled rotating magnetic dipole fields [4]. (a) Definition of parameters. (b) Π_1 value to maximize F for a given Π_3 value.

$$f_\theta(\rho,\theta) \approx 0 \quad (3)$$

$$f_\phi(\rho,\theta) = f_\phi(\rho,90°)\sin(\theta) \quad (4)$$

$$\tau_\rho(\rho,\theta) = \tau_\rho(\rho,0°)\cos(\theta) \quad (5)$$

$$\tau_\theta(\rho,\theta) = \tau_\theta(\rho,90°)\sin(\theta) \quad (6)$$

$$\tau_\phi(\rho,\theta) = 0. \quad (7)$$

Going beyond the force–torque induced by a single rotating dipole, in [4] we considered the open-loop attraction of conductive nonmagnetic objects by two dipoles rotating at the same speed in opposite directions. We characterized attraction along the axis of symmetry (e.g., y-axis) depicted and parameterized in Fig. 3(a). Since our force–torque model described previously does not currently allow for superposition, we do not actually actuate both field sources simultaneously. Rather, we duty cycle them such that they are each actuated for half of the time. The resultant attractive force (i.e., in the $-y$ direction) is

$$F = f_\phi(\rho,90°)\cos(\phi) - f_\rho(\rho,90°)\sin(\phi). \quad (8)$$

We formed a new nondimensional dependent parameter to characterize F, $\Pi_0 = Fr^4\mu^{-1}m^{-2}$, analogous to how we previously nondimensionalized forces. We also had to introduce a new nondimensional independent parameter: $\Pi_3 = y/\lambda = \tan(\phi)$, where Π_3 can take on any positive value. We found that the value of Π_1 that maximizes Π_0 (i.e., maximizes F) is only a function of Π_3 [see Fig. 3(b)], although the magnitude of the resulting Π_0 is also a function of Π_2. We observe that $\Pi_1 = 3.00$ is optimal in the limit as $\Pi_3 \to 0$ (i.e., at the midpoint between the rotating dipoles); this assumes that the (maximum) magnitude of m is invariant to ω, which will not be the case for electromagnetic

field sources. It is worth noting that, in [1], which considered dexterous manipulation of conductive nonmagnetic objects surrounded by dipole field sources, it was proposed that $\Pi_1 \approx 3$ was near optimal, based on simplifying assumptions.

III. Position Control

As depicted in Fig. 1, we are interested in controlling the position of conductive nonmagnetic objects in a workspace centered at the midpoint between two field sources. We define a coordinate frame such that the x-axis is pointing toward one of the field sources, which we designate as being at the $+x$ position, and away from the other field source, which we designate as being at the $-x$ position. The y-axis and z-axis should form a right-handed coordinate frame with the x-axis, but their choice is otherwise arbitrary.

Because we are interested in controlling the position $\boldsymbol{x}$ of a free-floating mass M, our plant has simple dynamics

$$\begin{bmatrix} \dot{\boldsymbol{x}}(t) \\ \ddot{\boldsymbol{x}}(t) \end{bmatrix} = \begin{bmatrix} \mathbb{0} & \mathbb{I} \\ \mathbb{0} & \mathbb{0} \end{bmatrix} \begin{bmatrix} \boldsymbol{x}(t) \\ \dot{\boldsymbol{x}}(t) \end{bmatrix} + \begin{bmatrix} \mathbb{0} \\ \frac{1}{M}\mathbb{I} \end{bmatrix} \boldsymbol{f}(t) \tag{9}$$

where $\mathbb{0}$ is a 3×3 zero matrix, $\mathbb{I}$ is a 3×3 identity matrix, and we use the dot notation to denote time derivatives. If we assume that our input force $\boldsymbol{f}(t)$ is updated with a sampling period T and held approximately constant for a given sampling period, we arrive at a sampled-data approximation of our plant

$$\begin{bmatrix} \boldsymbol{x}[k+1] \\ \dot{\boldsymbol{x}}[k+1] \end{bmatrix} = \begin{bmatrix} \mathbb{I} & T\mathbb{I} \\ \mathbb{0} & \mathbb{I} \end{bmatrix} \begin{bmatrix} \boldsymbol{x}[k] \\ \dot{\boldsymbol{x}}[k] \end{bmatrix} + \begin{bmatrix} \frac{T^2}{2M}\mathbb{I} \\ \frac{T}{M}\mathbb{I} \end{bmatrix} \boldsymbol{f}[k]. \tag{10}$$

We will implement a simple controller based on the error between the desired position $\boldsymbol{x}_{\text{des}}$ and the current position, with the addition of virtual damping, which is equivalent to state feedback with a reference input [18]

$$\begin{aligned} \boldsymbol{f}[k] &= k_p \left(\boldsymbol{x}_{\text{des}}[k] - \boldsymbol{x}[k]\right) - k_d \dot{\boldsymbol{x}}[k] \\ &= k_p \boldsymbol{x}_{\text{des}}[k] - \begin{bmatrix} k_p & k_d \end{bmatrix} \begin{bmatrix} \boldsymbol{x}[k] \\ \dot{\boldsymbol{x}}[k] \end{bmatrix}. \end{aligned} \tag{11}$$

The resulting closed-loop dynamics are

$$\begin{aligned} \begin{bmatrix} \boldsymbol{x}[k+1] \\ \dot{\boldsymbol{x}}[k+1] \end{bmatrix} = &\begin{bmatrix} \left(1 - \frac{k_p T^2}{2M}\right)\mathbb{I} & \left(T - \frac{k_d T^2}{2M}\right)\mathbb{I} \\ -\frac{k_p T}{M}\mathbb{I} & \left(1 - \frac{k_d T}{M}\right)\mathbb{I} \end{bmatrix} \begin{bmatrix} \boldsymbol{x}[k] \\ \dot{\boldsymbol{x}}[k] \end{bmatrix} \\ &+ \begin{bmatrix} \frac{k_p T^2}{2M}\mathbb{I} \\ \frac{k_p T}{M}\mathbb{I} \end{bmatrix} \boldsymbol{x}_{\text{des}}[k] \end{aligned} \tag{12}$$

which has a characteristic equation of the form

$$\begin{aligned} z^2 + \left(\frac{k_p T^2 + 2k_d T - 4M}{2M}\right) z + \left(\frac{k_p T^2 - 2k_d T + 2M}{2M}\right) \\ = 0 \end{aligned} \tag{13}$$

which we can control through the choice of the controller gains k_p and k_d. For example, for a dynamic response with no overshoot, we would like positive real poles/eigenvalues α at the same location, with $0 \leq \alpha < 1$ for stability and with α as small as possible for a fast response, with a resulting characteristic equation

$$(z - \alpha)(z - \alpha) = z^2 - 2\alpha z + \alpha^2 = 0. \tag{14}$$

This design choice constrains our choice of k_p and k_d as

$$k_p(\alpha) = \frac{M}{T^2}\left(\alpha^2 - 2\alpha + 1\right) \tag{15}$$

$$k_d(\alpha) = \frac{M}{2T}\left(-\alpha^2 - 2\alpha + 3\right). \tag{16}$$

IV. Force Control

The closed-loop dynamics in (12) and (13) assumes that we are able to achieve the desired force from (11). Achieving a desired force $\boldsymbol{f}_{\text{des}}$ is the core contribution of this article, which we address in the following. Throughout, if $\boldsymbol{f}_{\text{des}}$ is unachievable, our goal will be to induce the force $\boldsymbol{f}$ with minimal error. Also, we will develop our force controllers at the nominal operating point $\boldsymbol{x}_{\text{des}} = \mathbf{0}$ (i.e., at the midpoint between the field sources).

A. Force Controller 1: Minimize Torque

Given some desired force $\boldsymbol{f}_{\text{des}}$, we can always decompose it as the components parallel to, and orthogonal to, the x-axis

$$\boldsymbol{f}_{\text{des}} = \boldsymbol{f}_{\text{des}\parallel} + \boldsymbol{f}_{\text{des}\perp} \tag{17}$$

where

$$\boldsymbol{f}_{\text{des}\parallel} = (\boldsymbol{f}_{\text{des}} \cdot \hat{\boldsymbol{\imath}}_x)\hat{\boldsymbol{\imath}}_x \tag{18}$$

$$\boldsymbol{f}_{\text{des}\perp} = \boldsymbol{f}_{\text{des}} - \boldsymbol{f}_{\text{des}\parallel}. \tag{19}$$

Note that there is no need to officially assign an arbitrary y- and z-direction for the workspace coordinate frame. We can develop independent solvers for the parallel and orthogonal force components, and then superimpose the results. We will show that it is possible to induce these forces without inducing a net parasitic torque on the object. As in our prior works, we will not operate multiple magnetic commands simultaneously, rather, we will duty cycle the commands so that each uses a fraction of the control cycle, with the result being that we achieve the desired force in a time-averaged sense.

1) Forces Parallel to the x-Axis: We begin by analyzing the ability of our system to induce a force parallel to the x-axis (i.e., $\boldsymbol{f}_{\text{des}\parallel}$). Because each active field source always generates a repulsive force component, there are exactly two ways to induce a force in the $+x$ direction (i.e., when $\boldsymbol{f}_{\text{des}\parallel} \cdot \hat{\boldsymbol{\imath}}_x > 0$), as depicted in Fig. 4. Both use the field source at the $-x$ position, but result in parasitic torques in different directions

$$\hat{\boldsymbol{\omega}}_{-x} = \hat{\boldsymbol{\imath}}_x \quad \Rightarrow \quad \hat{\boldsymbol{\tau}} = \hat{\boldsymbol{\imath}}_x \tag{20}$$

$$\hat{\boldsymbol{\omega}}_{-x} = -\hat{\boldsymbol{\imath}}_x \quad \Rightarrow \quad \hat{\boldsymbol{\tau}} = -\hat{\boldsymbol{\imath}}_x. \tag{21}$$

By using (20) for 50% of the time allocated to $\boldsymbol{f}_{\text{des}\parallel}$, and using (21) for the other 50%, the parasitic torques will cancel if the object stayed in the same location during the entire duty cycle. Since the object does move slightly during one duty cycle, the parasitic torques will only approximately cancel. It follows that net torque is approximately zero.

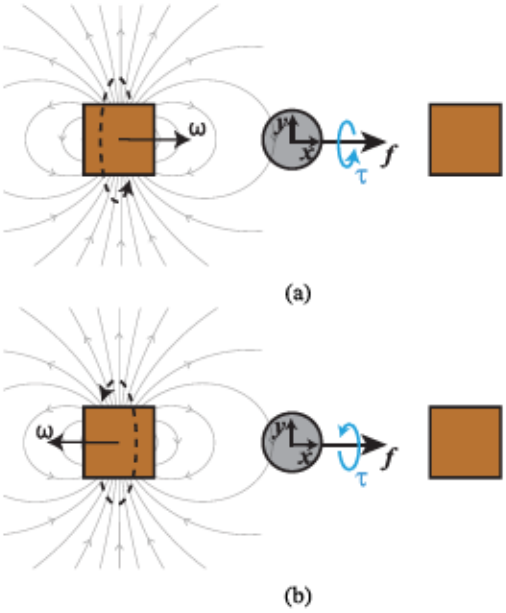

Fig. 4. Two configurations of rotating magnetic dipole fields to induce a force in the $+x$ direction; each induces a parasitic torque, but in opposite directions. Inducing forces in the $-x$ direction is done analogously, using the other field source. (a) Parasitic torque about $+x$ axis. (b) Parasitic torque about $-x$ axis.

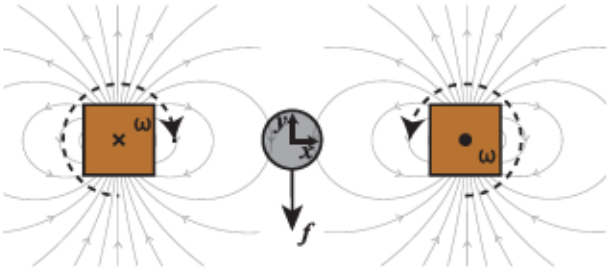

Fig. 5. Configuration of rotating magnetic dipole fields to induce a force in any direction orthogonal to the x-axis (shown here in the $-y$ direction, without loss of generality). This configuration results in no net torque.

Analogously, if we want to induce a force in the $-x$ direction (i.e., $\boldsymbol{f}_{\text{des}\parallel} \cdot \hat{\boldsymbol{i}}_x < 0$), we use the field source at the $+x$ position

$$\hat{\boldsymbol{\omega}}_{+x} = \hat{\boldsymbol{i}}_x \quad \Rightarrow \quad \hat{\boldsymbol{\tau}} = \hat{\boldsymbol{i}}_x \tag{22}$$

$$\hat{\boldsymbol{\omega}}_{+x} = -\hat{\boldsymbol{i}}_x \quad \Rightarrow \quad \hat{\boldsymbol{\tau}} = -\hat{\boldsymbol{i}}_x. \tag{23}$$

2) Forces Orthogonal to the x-Axis: Next, we consider the ability of our system to induce a force orthogonal to the x-axis (i.e., $\boldsymbol{f}_{\text{des}\perp}$), as depicted in Fig. 5. This can be thought of as a special case of our prior work [4] [see Fig. 3(a)], from which we know from symmetry that setting the two field sources to have equal dipole magnitudes and antiparallel angular velocities of equal magnitude will induce a force orthogonal to the x-axis

$$\hat{\boldsymbol{\omega}}_{-x} = \hat{\boldsymbol{i}}_x \times \hat{\boldsymbol{f}}_{\text{des}\perp} \tag{24}$$

$$\hat{\boldsymbol{\omega}}_{+x} = \hat{\boldsymbol{f}}_{\text{des}\perp} \times \hat{\boldsymbol{i}}_x. \tag{25}$$

By using (24) for 50% of the time allocated to $\boldsymbol{f}_{\text{des}\perp}$, and using (25) for the other 50%, the parasitic torques will cancel, such that the net torque is zero.

3) Achieving a Desired (Net) Force: We will denote the actual forces that our system induces as $\boldsymbol{f}_\parallel$ and $\boldsymbol{f}_\perp$. We will denote the duty cycle for each force component as $\delta_\parallel$ and $\delta_\perp$, where $\delta_\parallel + \delta_\perp = 1$ and it is understood that each of these duty cycles will be further divided in half to implement the respective force component as already described. The resultant net force is then

$$\boldsymbol{f} = \boldsymbol{f}_\parallel \delta_\parallel + \boldsymbol{f}_\perp \delta_\perp. \tag{26}$$

As described in Section II, the magnitude of the induced force is a function of the strength m and rotation frequency ω of the dipole fields. For electromagnets, we can control both of these terms independently, but their maximum values are coupled for any real electromagnetic field source. We can design the (m, ω) pair that will induce the maximum achievable force in a given direction, or that will achieve a desired force most efficiently (i.e., that minimizes m, which is generated with electricity); regardless, this is a relatively simple search over the model. We can also simply use some constant ω and treat m as the control variable, as we have in our prior works [1], [3], and [4], in which case the largest forces are simply induced by the largest m that is achievable at that ω. Let us simply assume that we have determined the maximum force magnitudes that we can achieve in the two orthogonal directions, and denote the resulting forces as $\overline{\boldsymbol{f}}_\parallel$ and $\overline{\boldsymbol{f}}_\perp$.

To solve for the duty cycles, let us imagine a case in which our induced force is in the correct direction (i.e., $\hat{\boldsymbol{f}} = \hat{\boldsymbol{f}}_{\text{des}}$), and its magnitude is so large that it is maximizing both of the force components simultaneously. The result is the largest force that we could possibly achieve in the desired direction

$$\overline{\boldsymbol{f}} = \overline{\boldsymbol{f}}_\parallel \delta_\parallel + \overline{\boldsymbol{f}}_\perp \delta_\perp \quad \text{where} \quad \hat{\overline{\boldsymbol{f}}} = \hat{\boldsymbol{f}}_{\text{des}}. \tag{27}$$

The associated duty cycles are unique, and they are optimal in the sense of balancing the force components with respect to what is achievable. Continuing with this thought experiment, we can solve for these duty cycles as

$$\delta_\parallel = \frac{\|\boldsymbol{f}_{\text{des}\parallel}\| \|\overline{\boldsymbol{f}}_\perp\|}{\|\boldsymbol{f}_{\text{des}\perp}\| \|\overline{\boldsymbol{f}}_\parallel\| + \|\boldsymbol{f}_{\text{des}\parallel}\| \|\overline{\boldsymbol{f}}_\perp\|} \tag{28}$$

$$\delta_\perp = 1 - \delta_\parallel \tag{29}$$

from which we can now solve (27) explicitly.

In general, we will not be requesting exactly $\|\boldsymbol{f}_{\text{des}}\| = \|\overline{\boldsymbol{f}}\|$. If $\|\boldsymbol{f}_{\text{des}}\| > \|\overline{\boldsymbol{f}}\|$, we will have to clip it to $\|\boldsymbol{f}_{\text{des}}\| = \|\overline{\boldsymbol{f}}\|$, since the requested value is unachievable. If $\|\boldsymbol{f}_{\text{des}}\| < \|\overline{\boldsymbol{f}}\|$, our decision will depend on if our field sources are electromagnets or permanent magnets. In the case of electromagnets, we will simply reduce the values of m that would be used to achieve the two components of $\overline{\boldsymbol{f}}$, assuming ω remains constant, since m affects forces quadratically

$$m_\parallel = \overline{m}_\parallel \sqrt{\frac{\|\boldsymbol{f}_{\text{des}}\|}{\|\overline{\boldsymbol{f}}\|}}, \quad m_\perp = \overline{m}_\perp \sqrt{\frac{\|\boldsymbol{f}_{\text{des}}\|}{\|\overline{\boldsymbol{f}}\|}}. \tag{30}$$

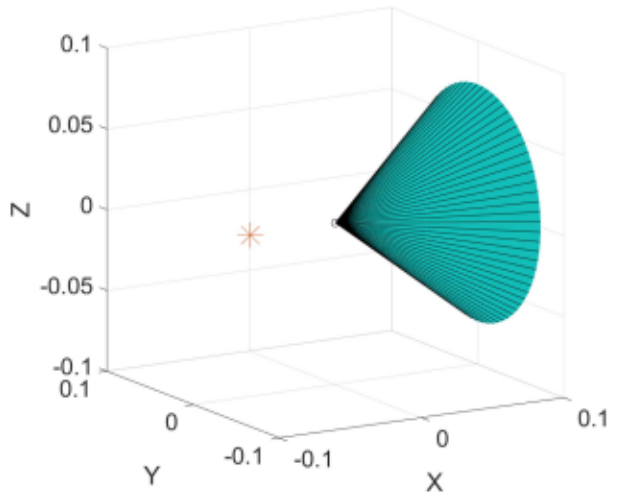

Fig. 6. Cone representing all possible force directions that can be induced by the field source at the $-x$ position (represented by an $*$) on a conductive object at the center of the workspace. The cone angle is dependent only on Π_1.

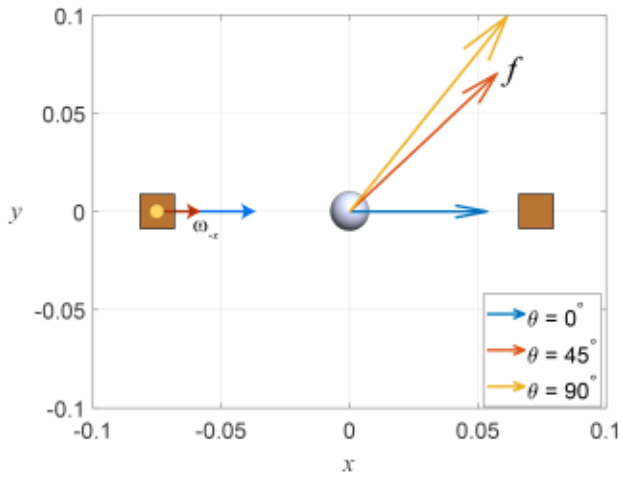

Fig. 7. Resultant forces created by a single magnetic dipole rotating at three different θ values. Arrows on the spherical object depict forces (which are all in the x–y plane), and corresponding colored arrows on the field source depict the associated $\boldsymbol{\omega}$ (which are all in the x–z plane, shown with perspective). The force created when $\theta = 90°$, depicted with a yellow arrow, is at an angle $\psi_{\theta=90°}$ measured from $\hat{\boldsymbol{i}}_x$.

In the case of permanent magnets, m is constant, and we must reduce ω by an appropriate amount using numerical techniques with the model of Section II.

B. Force Controller 2: Maximize Force

Let us assume that we have determined the maximum force magnitude that we can achieve in the x direction, and denote the resulting force as $\overline{\boldsymbol{f}}_{\parallel}$. If we utilize the same (m, ω) that produces this force, but orient $\boldsymbol{\omega}$ orthogonal to the x-axis rather than the parallel to it, we will induce a force that can be decomposed into a parallel component and an orthogonal component similar to what was done to a desired force in (17). For reasons that will become clear, we will denote this force as $\boldsymbol{f}_{\text{cone}}$. In this configuration, we are operating at $\theta = 90°$ (see Fig. 2). It then follows from (2) and (4) that:

$$\boldsymbol{f}_{\text{cone}\parallel} = \boldsymbol{f}_{\rho}(\rho, 90°) \tag{31}$$

$$\boldsymbol{f}_{\text{cone}\perp} = \boldsymbol{f}_{\phi}(\rho, 90°). \tag{32}$$

If $\boldsymbol{\omega}$ is then rotated about the x-axis, $\boldsymbol{f}_{\text{cone}\perp}$ will rotate about the x-axis by an equal amount. The total set of possible force vectors created by this process defines the outside of a cone, as shown in Fig. 6, with an angle

$$\psi_{\theta=90°} = \tan^{-1}\left(\frac{\|\boldsymbol{f}_{\text{cone}\perp}\|}{\|\boldsymbol{f}_{\text{cone}\parallel}\|}\right) \tag{33}$$

measured from $\hat{\boldsymbol{i}}_x$. If $\boldsymbol{\omega}$ is rotated toward $\hat{\boldsymbol{i}}_x$ (i.e., if θ varies from 90° to 0°) or if $\boldsymbol{\omega}$ is rotated toward $-\hat{\boldsymbol{i}}_x$ (i.e., if θ varies from 90° to 180°), both $\|\boldsymbol{f}_{\text{cone}\perp}\|$ and ψ go to 0, as shown in Fig. 7. This effectively fills in the rest of the cone. Therefore, the field source at the $-x$ position can generate a force with any $0 \leq \psi \leq \psi_{\theta=90°}$ measured from $\hat{\boldsymbol{i}}_x$. Analogously, the field source at the $+x$ position can generate a force with any $0 \leq \psi \leq \psi_{\theta=90°}$ measured from $-\hat{\boldsymbol{i}}_x$.

If we again decompose some desired force into its components parallel to, and orthogonal to, the x-axis as in (17), we can conclude that our system is capable of producing a force in the direction of $\boldsymbol{f}_{\text{des}}$ using only a single rotating magnetic dipole source if

$$\frac{\|\boldsymbol{f}_{\text{des}\perp}\|}{\|\boldsymbol{f}_{\text{des}\parallel}\|} < \frac{\|\boldsymbol{f}_{\text{cone}\perp}\|}{\|\boldsymbol{f}_{\text{cone}\parallel}\|}. \tag{34}$$

The foundation of the force controller of this section is as follows: if the desired force $\boldsymbol{f}_{\text{des}}$ is within one of the two achievable cones, then we should use the respective field source with a 100% duty cycle to achieve it. This strategy will be very efficient at generating forces by capitalizing on the natural force-generation properties of a single rotating magnetic dipole. However, it will likely generate some parasitic torque on the object as well.

1) Forces Inside the Achievable Cone: If we keep ω and m constant at the pairing that produces our maximum parallel force, ψ will be a function of only θ. If we can produce a force in the desired direction [i.e., if (34) is true] then we use a simple solver to determine the θ from (2) and (4) that solves

$$\frac{\|\boldsymbol{f}_{\phi}(\rho, \theta)\|}{\|\boldsymbol{f}_{\rho}(\rho, \theta)\|} = \frac{\|\boldsymbol{f}_{\text{des}\perp}\|}{\|\boldsymbol{f}_{\text{des}\parallel}\|}. \tag{35}$$

By utilizing a single field source rotating at an angle θ determined from (34), the resultant force $\overline{\boldsymbol{f}}$ will be in the desired direction. If $\|\boldsymbol{f}_{\text{des}}\| > \|\overline{\boldsymbol{f}}\|$ we will again have to clip it. If $\|\boldsymbol{f}_{\text{des}}\| < \|\overline{\boldsymbol{f}}\|$ then our decision will again depend on if our field sources are electromagnets or permanent magnets.

For electromagnets, m is variable and effects only the resultant force magnitude, not its direction. If $\|\boldsymbol{f}_{\text{des}}\| > \|\overline{\boldsymbol{f}}\|$, we will have to clip our desired force to $\|\boldsymbol{f}_{\text{des}}\| = \|\overline{\boldsymbol{f}}\|$. If $\|\boldsymbol{f}_{\text{des}}\| < \|\overline{\boldsymbol{f}}\|$, we will simply reduce the value of m to achieve the desired force

$$m = \overline{m}\sqrt{\frac{\|\boldsymbol{f}_{\text{des}}\|}{\|\overline{\boldsymbol{f}}\|}}. \tag{36}$$

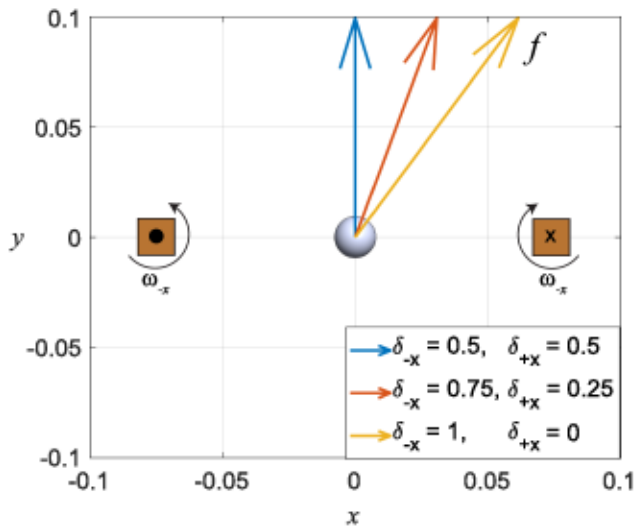

Fig. 8. Effect on the resultant force vector as the duty cycle of the two field sources is varied from 50%/50% to 100%/0%. Arrows on the spherical object depict forces (which are all in the x–y plane). Arrows on the field sources depict the associated $\boldsymbol{\omega}$ (which are always parallel or antiparallel to the z-axis). The force created when the duty cycle is 100%/0%, depicted with a yellow arrow, is at an angle $\psi_{\theta=90^\circ}$ measured from $\hat{\boldsymbol{i}}_x$.

For permanent magnets the only variable we can modify is $\boldsymbol{\omega}$. The angle with respect to $\hat{\boldsymbol{i}}_x$ of our resultant force is

$$\psi(\omega,\theta) = \tan^{-1}\left(\frac{\boldsymbol{f}_\phi(\rho,\theta)}{\boldsymbol{f}_\rho(\rho,\theta)}\right) \tag{37}$$

which is a function of ω and θ. Therefore, if we scale back the frequency in order to lower our force magnitude to some desired force magnitude the resultant force direction will also change. We would therefore need to search over the (ω,θ) search-space for a solution that will ensure the resultant force matches the desired force in both direction and magnitude.

2) Forces Outside the Achievable Cone: A rotating dipole field will always create a force in the $\boldsymbol{\rho}$ direction, therefore, $\psi_{\theta=90^\circ}$ is always less than 90°. Forces in a direction beyond $\psi_{\theta=90^\circ}$ (i.e., $\psi_{\theta=90^\circ} < \psi \leq 90^\circ$) are not achievable with a single rotating dipole field. However, we know that if we rotate the two dipoles according to (24) and (25) with a 50%/50% duty cycle the resulting force will be entirely orthogonal to the x-axis (i.e., will achieve $\psi = 90^\circ$). By varying the duty cycle, we can produce forces outside the cone created by a single rotating dipole field, as shown in Fig. 8. Determining the correct duty cycle δ_{-x} and δ_{+x} for the field sources at the $-x$ and $+x$ positions, respectively, where $\delta_{-x} + \delta_{+x} = 1$, depends on whether the system is utilizing electromagnets or permanent magnets.

For electromagnets, m is variable and effects only the resultant force magnitude, not its direction. We can therefore determine the duty cycle that results in a force in the desired direction, independent of magnitude. We use a numeric optimizer to solve a problem of the form

$$\begin{aligned} \underset{\delta_{-x}}{\arg\min} \quad & \left\| \hat{\boldsymbol{f}}_{\text{des}} - \hat{\boldsymbol{f}} \right\|^2 \\ \text{s.t.} \quad & \boldsymbol{f} = \delta_{-x}\boldsymbol{f}_{-x} + (1-\delta_{-x})\boldsymbol{f}_{+x} \end{aligned} \tag{38}$$

where $\boldsymbol{f}_{-x}$ and $\boldsymbol{f}_{+x}$ are the resultant forces from the field sources at the $-x$ and $+x$ positions, respectively, which are precomputed offline by implementing the dipole rotation axes defined by (24) and (25) using the (m,ω) pair that will induce the maximum achievable force. The resulting optimal duty cycle will result in $\boldsymbol{f} = \overline{\boldsymbol{f}}$, the maximum achievable force in the desired direction. If $\|\boldsymbol{f}_{\text{des}}\| > \|\overline{\boldsymbol{f}}\|$, we will have to clip it to $\|\boldsymbol{f}_{\text{des}}\| = \|\overline{\boldsymbol{f}}\|$. If $\|\boldsymbol{f}_{\text{des}}\| < \|\overline{\boldsymbol{f}}\|$, and assuming ω remains constant, we simply reduce m as in (36).

For permanent magnets, the dipole strength is set, but $\boldsymbol{\omega}$ can be modified. We will still choose the direction of $\boldsymbol{\omega}$ defined by (24) and (25). Because ω effects not only the resultant force magnitude but also the resultant force direction, we need to couple these in the optimization

$$\begin{aligned} \underset{\omega,\delta_{-x}}{\arg\min} \quad & \|\boldsymbol{f}_{\text{des}} - \boldsymbol{f}\|^2 \\ \text{s.t.} \quad & \boldsymbol{f} = \delta_{-x}\boldsymbol{f}_{-x} + (1-\delta_{-x})\boldsymbol{f}_{+x} \\ & \omega \leq \omega_{\max} \end{aligned} \tag{39}$$

where $\boldsymbol{f}_{-x}$ and $\boldsymbol{f}_{+x}$ are the resultant forces from the field sources at the $-x$ and $+x$ positions, respectively, calculated online using (2) and (4) for the particular (m,ω) pair.

3) Parasitic Torque: By minimizing the number of distinct rotating-dipole-field actions to generate a desired force, we minimize the generation of wasted opposing forces whose sole purpose is to cancel each other out. This enables the system to achieve a larger maximum force, but at the cost of parasitic torque. Forces and torques for a single rotating dipole field as a function of θ are shown in Fig. 9. Because the forces are symmetric about $\theta = 90^\circ$, the resultant force generated at some θ is the same if we instead rotate the dipole field source at $\theta^* = 180^\circ - \theta$. For forces produced inside of $\psi_{\theta=90^\circ}$ (i.e., inside the cone), since the torque in the x-direction is mirrored about $\theta = 90^\circ$, we can alternate the field rotation between θ and θ^* with a 50%/50% duty cycle to cancel out the x-component of torque. However, the torque produced in the $\boldsymbol{\rho} \times \hat{\boldsymbol{f}}_{\text{des}\perp}$ direction cannot be removed with such a process, and is considered parasitic torque. For forces produced outside of $\psi_{\theta=90^\circ}$, the torques produced by each rotating dipole field are in equal and opposite directions and are both orthogonal to the x-axis, however because one is given a larger portion of the duty cycle, the torques will not be equal in magnitude thus leaving some parasitic torque, which is again in the $\boldsymbol{\rho} \times \hat{\boldsymbol{f}}_{\text{des}\perp}$ direction of the rotating dipole field.

C. Comparison of Force Controllers

The two force controllers described previously, each offer their own advantages and disadvantages. The minimize-torque controller is straightforward to solve numerically, it is efficient in that it utilizes the entire control cycle to perform manipulation, and it results in no net torque (at least nominally). However, it artificially limits our choice of $\boldsymbol{\omega}$ to being either parallel or orthogonal to the x-axis. Alternatively, the maximize-force controller is very good at achieving a desired force using a single field source when possible, which is energy-efficient.

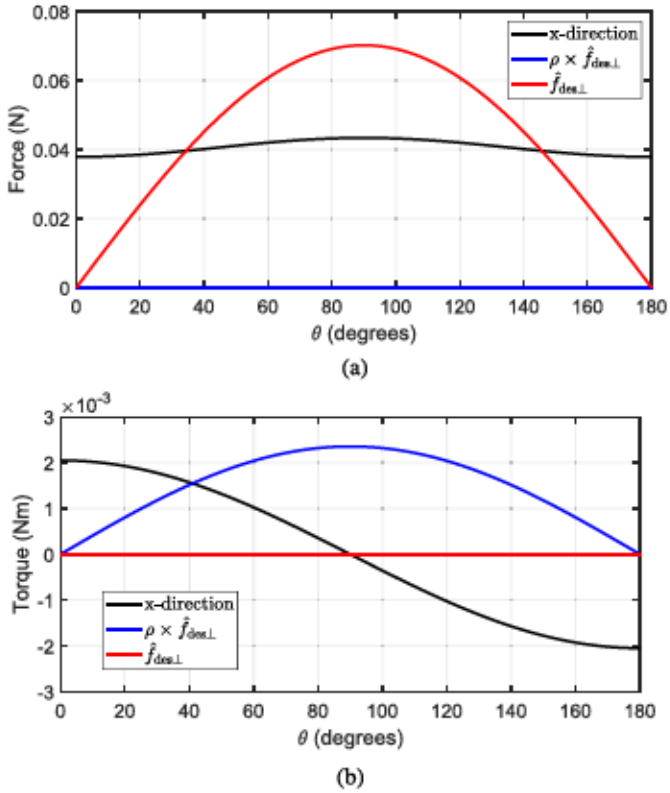

Fig. 9. Magnitude of the resultant (a) force and (b) torque components as a function of θ for a 25 mm radius copper sphere placed 80 mm away from a single dipole field rotating at $\omega = 15$ Hz with $m = 40$ A $\cdot$ m^2. (a) Forces. (b) Torques.

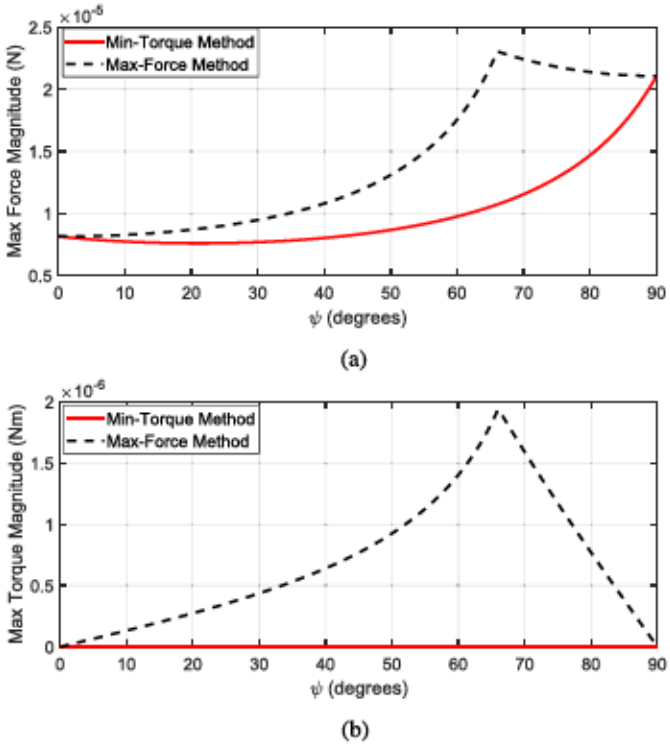

Fig. 10. Comparison of (a) the maximum possible force produced and (b) the corresponding parasitic torque, for the minimize-torque controller and the maximize-force controller, as a function of ψ measured from the x-axis for a 20 mm radius copper sphere placed $\lambda = 222.5$ mm away from two dipole fields rotating at $\omega = 15$ Hz with $m = 40$ A $\cdot$ m^2.

Fig. 10 provides a comparison of the forces and torques produced as a function of the angle ψ of $\boldsymbol{f}_{\text{des}}$ measured from the x-axis

$$\psi = \tan^{-1}\left(\frac{\|\boldsymbol{f}_{\text{des}\perp}\|}{\|\boldsymbol{f}_{\text{des}\parallel}\|}\right). \tag{40}$$

For desired forces that are either parallel or orthogonal to the x-axis, the two methods result in the same maximum achievable force and the same corresponding parasitic torque. For other force directions, the maximize-force controller is capable of producing larger forces—in some cases, substantially larger. The minimize-torque controller is capable of producing a force in any direction without the generation of any parasitic torque. It is worth noting that the discontinuity in the results for the maximize-force controller occurs at $\psi_{\theta=90^\circ}$ and, at least for our parameter values, it was at this discontinuity that we observed the largest difference between the two methods.

V. Experimental Verification

A. Numerical Simulations

1) Methods: In order to verify the ability of our proposed controllers to regulate the position of an object to the midpoint between two field sources, we created a 6-DOF numerical simulation of a free-floating sphere described by dynamics

$$M\ddot{\boldsymbol{x}} = \boldsymbol{f} \tag{41}$$

$$\mathbb{J}\dot{\boldsymbol{\omega}} + \boldsymbol{\omega} \times \mathbb{J}\boldsymbol{\omega} = \boldsymbol{\tau} \tag{42}$$

where $\boldsymbol{f}$ and $\boldsymbol{\tau}$ are the eddy-current-induced force and torque, respectively, as described in Section II, and

$$\mathbb{J} = \frac{2}{5}Mr^2\mathbb{I} \tag{43}$$

is the moment-of-inertia tensor of a solid sphere. The Coriolis term in (42) has no effect due to the symmetry of $\mathbb{J}$, so we eliminate it going forward. We numerically integrate with a period of T_{ni}

$$\begin{bmatrix}\boldsymbol{x}[k+1]\\ \dot{\boldsymbol{x}}[k+1]\\ \boldsymbol{\omega}[k+1]\end{bmatrix} = \begin{bmatrix}\mathbb{I} & T_{\text{ni}}\mathbb{I} & \mathbb{0}\\ \mathbb{0} & \mathbb{I} & \mathbb{0}\\ \mathbb{0} & \mathbb{0} & \mathbb{I}\end{bmatrix}\begin{bmatrix}\boldsymbol{x}[k]\\ \dot{\boldsymbol{x}}[k]\\ \boldsymbol{\omega}[k]\end{bmatrix} + \begin{bmatrix}\frac{T_{\text{ni}}^2}{2M}\mathbb{I} & \mathbb{0}\\ \frac{T_{\text{ni}}}{M}\mathbb{I} & \mathbb{0}\\ \mathbb{0} & T_{\text{ni}}\mathbb{J}^{-1}\end{bmatrix}\begin{bmatrix}\boldsymbol{f}[k]\\ \boldsymbol{\tau}[k]\end{bmatrix}. \tag{44}$$

We chose parameters that approximate those of our physical experiments (see Section V-B). The two field sources are modeled as point dipoles that rotate with an angular velocity $\omega = 15$ Hz with a maximum strength of $m = 40$ A $\cdot$ m^2, and are placed 445 mm apart (i.e., at $\lambda = \pm 222.5$ mm along the x-axis). An aluminum sphere (conductivity $\sigma = 3.69 \times 10^7$ S/m and density $\rho = 2710$ kg/m^3) with a radius of 20 mm is placed a distance $\lambda/4 = 55$ mm away from the origin of the coordinate system

TABLE III
COMPARISON OF THE MEDIAN SIMULATED SETTLING TIME, NORMALIZED PATH LENGTH, AND FINAL ANGULAR VELOCITY OF THE MINIMIZE-TORQUE CONTROLLER, MAXIMIZE-FORCE CONTROLLER, AND GREEDY CONTROLLER WITH $q = 0$, $q = 1$, AND $q = 3$, USING A GENTLE POSITION CONTROLLER ($\alpha = 0.99$) AND ONE THAT IS APPROXIMATELY $3\times$ MORE AGGRESSIVE ($\alpha = 0.97$)

		Min-torque	Max-force	Greedy, $q = 0$	Greedy, $q = 1$	Greedy, $q = 3$
Settling time	$\alpha = 0.97$	1.46	1.04	1.04	*	1.41
	$\alpha = 0.99$	1.45	1.05	1.05	*	1.41
Normalized path length	$\alpha = 0.97$	1.09	*	*	1.02	1.07
	$\alpha = 0.99$	1.08	*	*	1.01	1.07
Final angular velocity	$\alpha = 0.97$	*	9.14	11.58	9.33	9.29
	$\alpha = 0.99$	*	9.10	10.06	9.08	9.79

For each metric, the lowest (i.e., best) value is denoted with an *, and the values of the other controllers are shown as multiples of the respective lowest value.

(which is located at the midpoint between the field sources) along the $\pm x$, y, and z axes, as well as toward the corners of the eight octants made by the coordinate system, for a total of 14 initial conditions distributed around the surface of a sphere. Starting from rest, the object is commanded to move to the origin of the coordinate system (i.e., $\boldsymbol{x}_{\text{des}} = \mathbf{0}$). The control law from (11) is used, where k_p and k_d are functions of the pole/eigenvalue α as in (15) and (16). We performed simulations with $\alpha = 0.99$, which provides a gentle dynamic response, as well as with $\alpha = 0.97$, which is approximately three times more aggressive. We implemented a sampling period of $T = 1$ s: each controller measures the state of the object once every second, uses that state to determine a desired force, then attempts to create that force by subdividing the next second in whole increments of T_{ni} using its own particular algorithm. We numerically integrated with $T_{\text{ni}} = 1$ ms.

We also wanted to critically compare the performance of our proposed controllers to our current state-of-the-art wrench solver [3], which is a greedy optimization method that solves for the instantaneous wrench that most closely matches the desired wrench in terms of minimizing a weighted norm of the wrench error. The weighting matrix is of the form $\texttt{diag}\{1, 1, 1, q, q, q\}$, where $q = 0$ results in no weighting of the error in the torque vector (i.e., pure force control), and an increase in q corresponds to an increase in the importance of torque error relative to force error. We explicitly consider $q = 0$, $q = 1$, and $q = 3$. We solve for the actuation commands to achieve a desired wrench with a sampling period of $T = 1$ s. The desired force is set by the same position controller described previously, and the desired torque is always set to zero. This method also requires initial estimates to seed the solver; we chose 14 different initial estimates to help ensure that we found an optimal solution using an off-the-shelf least-squares solver. With this solver we found the two initial estimates indicated by Tabor et al. [3] to be insufficient, this is likely highly dependent on their choice of optimization algorithm.

We use three metrics to quantify the quality of the responses: settling time, normalized path length, and final angular velocity. The settling time gives a sense for how quickly the controller is able to move an object to a position setpoint. We define the settling time as the time at which the center of the object enters a spherical region that has a radius that is 1% of the total step size of 111.25 mm, and then never leaves that spherical region. The normalized path length is defined as the distance traveled by the object from the start of the trial to the settling time, normalized by the shortest possible distance (i.e., 99% of the total step size of 111.25 mm). This metric captures both nonstraight paths and overshoot. The final angular velocity captures the amount of net parasitic torque induced on the object, given that, in all cases, the goal was to induce no torque during the position-regulation task. For all three metrics, smaller values are better.

2) Results and Discussion: The results of our simulations are presented in Fig. 11 in the form of box-whisker plots of the 14 trials per controller. We present a critical comparison of the median results in Table III and Supplemental Video 1.

As we make our position controller more aggressive by decreasing α, the settling time decreases by a factor of three (approximately); this is as expected. As we make our position controller more aggressive, we also observe an increase in the final angular velocity and the average normalized path length. The increase to path length is due to some slight overshoot when trying to reach the goal more aggressively. The increase in the final angular velocity is due to the controller asking for larger forces, which leads to a corresponding increase in parasitic torque.

The minimize-torque controller is an order-of-magnitude better than the other controllers at not inducing parasitic torque on the object, measured via its final angular velocity. This comes at the cost of longer settling times and slightly longer path lengths.

With the greedy controller, as we increase q (i.e., penalize torque more) there is a decrease in the final angular velocity as expected, but with a ceiling effect. However, increasing q too high substantially harms the performance of the position control. We found that $q = 3$ gives similar median performance as the minimize-torque controller in terms of settling time and normalized path length. Further increases in q only led to negative changes in performance without any corresponding positive changes.

The maximize-force controller and the greedy controller with $q = 0$ perform equally well in terms of moving objects from across the workspace along the shortest-possible straight-line path to the setpoint. However, the maximize-force controller performs slightly better in terms of both settling time and not inducing parasitic torque.

One thing that we observed that was unexpected was that setting $q = 1$ with the greedy controller resulted in a median settling time that is slightly lower (i.e., faster) than with $q = 0$, with some trials that are much lower. This is best explained as follows. The greedy solver with $q = 1$ sometimes struggles to exactly produce the desired force because it is also explicitly trying to create no torque, which leads to a dynamic response that deviates from the idealized response anticipated by the

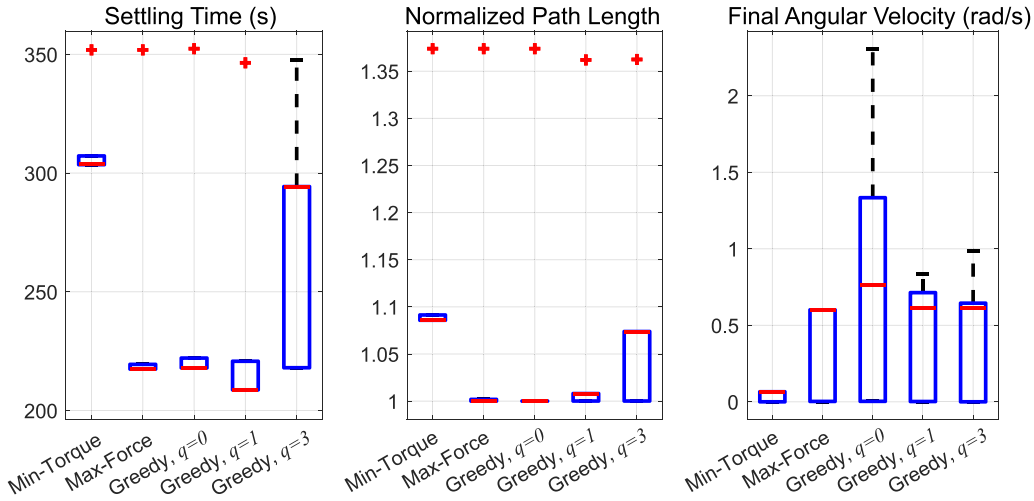

(a)

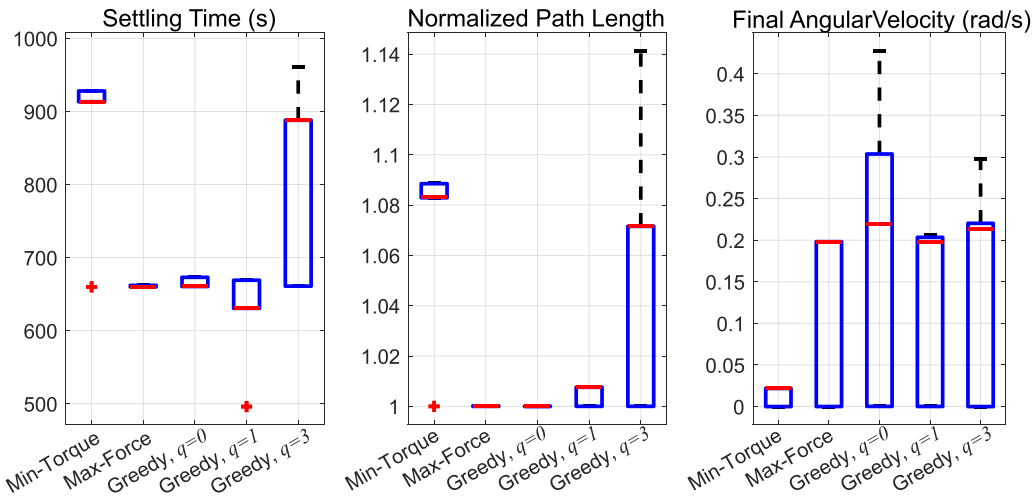

(b)

Fig. 11. Box-whisker plots comparing the simulated settling time, normalized path length, and final angular velocity of the minimize-torque controller, the maximize-force controller, and the greedy controller with $q = 0, q = 1$, and $q = 3$, using (b) a gentle position controller ($\alpha = 0.99$) and (a) one that is approximately $3\times$ more aggressive ($\alpha = 0.97$). Each box-whisker plot comprises 14 trials with starting locations that are all at a distance $\rho = \lambda/4$ from the setpoint.

position controller. In some cases, this actually leads to a more aggressive response that overshoots the setpoint (which explains the increase in normalized path length); if the overshoot is not sufficient to leave the 1% sphere around the setpoint, this actually results in a decrease in 1% settling time. Thus, we are not inclined to interpret the faster response in a positive way, since it indicates a lack of control.

B. Physical Experiments

1) Methods: For an experimental verification of the position controllers performance, we created an experimental setup comprising two Omnimagnets [19] of the design originally described in [20]; these are the same Omnimagnets used in our previous works on this topic [1], [3]. We placed the Omnimagnets 0.4 m apart ($\lambda = 0.2$ m), adjacent to a pool of water, as shown in in Fig. 12. We placed a solid aluminum sphere with a radius $r = 0.02$ m and mass 0.091 kg in a 3-D-printed (nonmagnetic and nonconductive) raft of diameter 88 mm floating on the surface of the water, which has a depth of 190 mm. The raft itself adds another 0.061 kg to the object's mass. The pose of the raft, and thus the aluminum sphere, was tracked using a fiducial marker. This setup provides a 3-DOF simulation of microgravity (two-degree-of-freedom translation in the horizontal plane and one-degree-of-freedom rotation about the vertical axis). The center of each Omnimagnet, which is the location of the magnetic dipole that it creates, was placed at the same vertical height as the center of the aluminum sphere, which is just below the surface of the water, such that experiments are conducted in the $z = 0$ plane depicted in Fig. 1.

The aluminum sphere was commanded to one of three starting locations located 50 mm away from the center of the workspace

TABLE IV
COMPARISON OF THE MEDIAN EXPERIMENTAL SETTLING TIME, NORMALIZED PATH LENGTH, AND FINAL ANGULAR VELOCITY OF THE MINIMIZE-TORQUE CONTROLLER, THE MAXIMIZE-FORCE CONTROLLER, AND THE GREEDY CONTROLLER WITH $q = 0$ AND $q = 1$, WITH $\alpha = 0.97$

	Min-torque	Max-force	Greedy, $q = 0$	Greedy, $q = 1$
Settling time	1.45	1.13	*	1.17
Normalized path length	1.11	1.02	*	1.13
Final angular velocity	*	8.33	11.00	13.17

For each metric, the lowest (i.e., best) value is denoted with an *, and the values of the other controllers are shown as multiples of the respective lowest value.

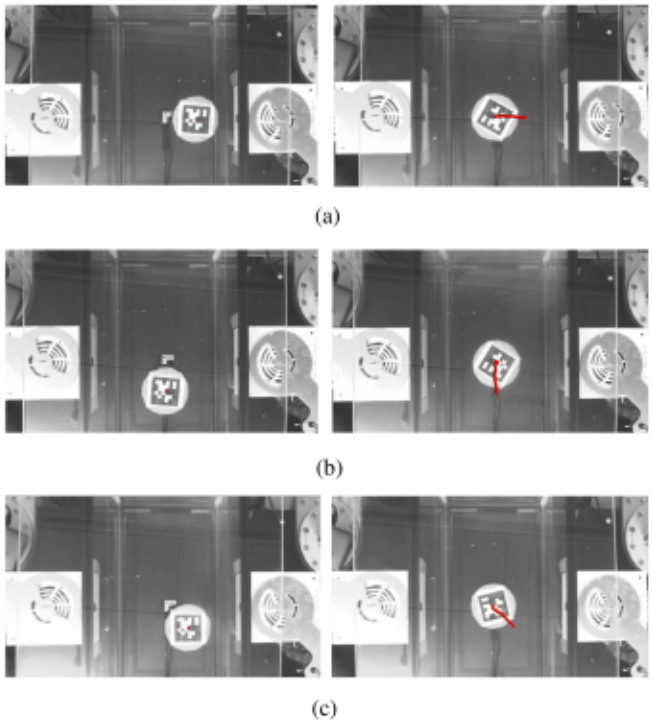

Fig. 12. Top-down view of the experimental setup comprising two Omnimagnets with centers placed 0.4 m apart surrounding a pool of water, with a raft carrying a 20 mm radius aluminum sphere, equipped with a fiducial marker. The left image shows the initial condition, and the right image shows the final condition with the path taken depicted in red, for typical runs. (a) $\boldsymbol{x}(0) = [50 \quad 0]^\top$ mm. (b) $\boldsymbol{x}(0) = [0 \quad -50]^\top$ mm. (c) $\boldsymbol{x}(0) = [25\sqrt{2} \quad -25\sqrt{2}]^\top$ mm.

$(x = y = 0)$ along the x-axis, the $-y$-axis and the axis 45° between the two, using the method described in [3]. Once the object was at rest in the given starting location, it was commanded to move to the center using the minimize-torque controller, the maximize-force controller, and the greedy controller from [3] with $q = 0$ and $q = 1$. Using the combined mass, we calculated the position controller gains as in (15) and (16), using $\alpha = 0.97$.

This experimental setup provides a reasonable approximation of the microgravity environment of space, but the results will be slightly different due to various inertial and drag effects of the water. We chose the more aggressive controller ($\alpha = 0.97$) due to the presence of unmodeled drag from the water. We heuristically found that reducing k_d (from the value calculated previously) by 25% to account for the unmodeled drag led to results that most closely matched our simulations.

2) Experimental Results: Typical trials of our experiment are shown in Fig. 13. The complete results are presented in Fig. 14 as a box-whisker plot of the nine trials per controller. Again, we present a critical comparison of the median experimental

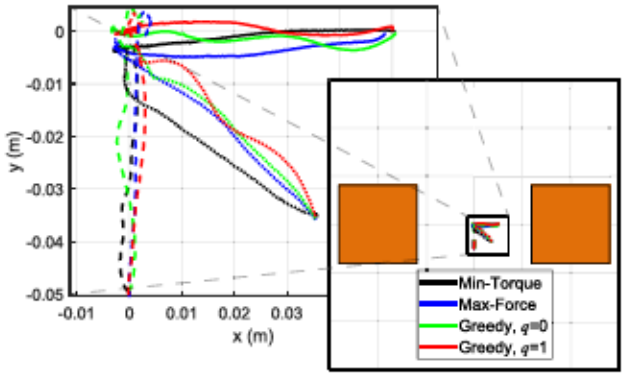

Fig. 13. Typical experimental runs for the minimize-torque controller, the maximize-force controller, and the greedy controller with $q = 0$ and $q = 1$, all using $\alpha = 0.97$. Results show position regulation for a 20 mm radius aluminum sphere starting from rest at a 50 mm distance along the x-axis, the $-y$-axis, and a diagonal axis. See Supplemental Video 2.

results in Table IV. Although the particular numerical values vary slightly from the simulation results due to the unmodeled effects of water, we observe the same general trends that we did in the simulations. The minimize-torque controller is again an order of magnitude better than the other methods at not inducing parasitic torque on the object; this again comes at the cost of longer settling times and slightly longer path lengths. The maximize-force controller and greedy controller with $q = 0$ both have the shortest path length and comparable settling times. Increasing the value of q again lowers the final angular velocity but come at the cost of higher settling times and path lengths. Considering the results in Table IV closely match those in Table III, we are confident that, although our water-based microgravity simulator adds some parasitic effects, our physical experiments reinforce the conclusions drawn from our simulations.

VI. DISCUSSION

As discussed earlier, our primary motivation for this work is the task of regulating the position of a resident space object at the midpoint between two field sources, to be detumbled by a secondary controller. When the object is already very near to the midpoint, it seems clear that the proposed minimize-torque controller is most desirable, in that it creates very little parasitic torque that may disturb the axis of rotation of the object. When the object is relatively far from the midpoint, the proposed maximize-force controller seems to be the best choice, although it performs quite comparably to our prior optimization-based greedy method.

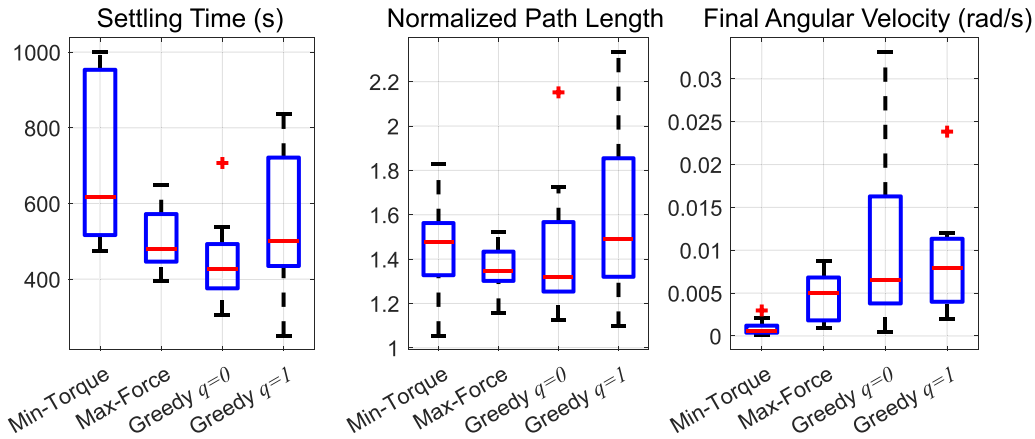

Fig. 14. Box-whisker plots comparing the experimental settling time, normalized path length, and final angular velocity of the minimize-torque controller, the maximize-force controller, and the greedy controller with $q = 0$ and $q = 1$, with $\alpha = 0.97$. Each box-whisker plot comprises nine trials with starting locations that are all at a distance $\rho = \lambda/4$ from the setpoint.

It is important to note that both the minimize-torque and maximize-force controllers were developed for the structured environment near the midpoint between two field sources; they are highly specialized for that configuration (which is important in our motivating application). There is no reason to believe that the positive results that we found will translate to other location outside of this nominal workspace.

We assumed a point dipole model for our field sources. This model is perfect for a spherical permanent magnets [21]. For cubic and cylindrical permanent magnets [21], as well as omnidirectional electromagnets [19], the model is accurate outside of approximately 1.5 minimum-bounding-sphere radii.

VII. Conclusion

In this article, we developed two new low-level 3-DOF force controllers, which we named the minimize-torque controller and the maximize-force controller, for the manipulation of conductive nonmagnetic objects in the nominal workspace between two rotating-magnetic-dipole field sources. We compared the two new force controllers with each other and with the state-of-the-art greedy controller from [3] (which is an improvement of the original controller in [1]), using the same high-level position controller, in the task of position regulation to the midpoint between the field sources. We found that the minimize-torque controller performs best (by an order of magnitude) in terms of not inducing parasitic angular momentum on the object, but at the cost of modestly longer settling times. We put a premium on not inducing parasitic angular momentum on the object because we are ultimately interested in applying this position regulator to the task of detumbling objects in space for on-orbit servicing or deorbiting.

Acknowledgment

This project is a collaboration with Rogue Space Systems.

References

[1] L. N. Pham, G. F. Tabor, A. Pourkand, J. L. B. Aman, T. Hermans, and J. J. Abbott, "Dexterous magnetic manipulation of conductive non-magnetic objects," *Nature*, vol. 598, pp. 439–443, 2021.
[2] J. J. Abbott, E. Diller, and A. J. Petruska, "Magnetic methods in robotics," *Annu. Rev. Control Robot. Auton. Syst.*, vol. 3, pp. 57–90, 2020.
[3] G. F. Tabor, L. N. Pham, J. J. Abbott, and T. Hermans, "Adaptive manipulation of conductive, nonmagnetic objects via a continuous model of magnetically induced force and torque," in *Proc. Robotics: Sci. Syst.*, 2022, pp. 1–11.
[4] D. K. Dalton, G. F. Tabor, T. Hermans, and J. J. Abbott, "Attracting conductive nonmagnetic objects with rotating magnetic dipole fields," *IEEE Robot. Autom. Lett.*, vol. 7, no. 4, pp. 11484–11491, Oct. 2022.
[5] J. N. Opiela, "A study of the material density distribution of space debris," *Adv. Space Res.*, vol. 43, no. 7, pp. 1058–1064, 2009.
[6] F. Sugai, S. Abiko, T. Tsujita, X. Jiang, and M. Uchiyama, "Detumbling an uncontrolled satellite with contactless force by using an eddy current brake," in *Proc. IEEE/RSJ Int. Conf. Intell. Robots Syst.*, 2013, pp. 783–788.
[7] N. Ortiz Gómez and S. J. I. Walker, "Eddy currents applied to de-tumbling of space debris: Analysis and validation of approximate proposed methods," *Acta Astronaut.*, vol. 114, pp. 34–53, 2015.
[8] R. C. Youngquist, M. A. Nurge, S. O. Starr, F. A. Leve, and M. Peck, "A slowly rotating hollow sphere in a magnetic field: First steps to de-spin a space object," *Am J. Phys.*, vol. 84, no. 3, pp. 181–191, 2016.
[9] M. A. Nurge, R. C. Youngquist, and S. O. Starr, "Drag and lift forces between a rotating conductive sphere and a cylindrical magnet," *Am J. Phys.*, vol. 86, no. 6, pp. 443–452, 2018.
[10] X. Liu, Y. Lu, Y. Zhou, and Y. Yin, "Prospects of using a permanent magnetic end effector to despin and detumble an uncooperative target," *Adv. Space Res.*, vol. 61, no. 8, pp. 2147–2158, 2018.
[11] X. Liu, Y. Lu, Q. Zhang, and K. Zhang, "An application of eddy current effect on the active detumble of uncontrolled satellite with tilt air gap," *IEEE Trans. Magn.*, vol. 55, no. 12, Dec. 2019, Art. no. 6201511.
[12] M. Shan, J. Guo, and E. Gill, "Review and comparison of active space debris capturing and removal methods," *Prog. Aerosp. Sci.*, vol. 80, pp. 18–32, 2016.
[13] C. P. Mark and S. Kamath, "Review of active space debris removal methods," *Space Policy*, vol. 47, pp. 194–206, 2019.
[14] K. T. Wilson, G. Bernal, and M. A. Peck, "Eddy-current actuator for attraction and repulsion of non-ferromagnetic, conductive spacecraft," *J. Spacecr. Rockets*, vol. 60, no. 4, pp. 1063–1071, 2023.
[15] B. Z. Reinhardt and M. A. Peck, "New electromagnetic actuator for on-orbit inspection," *J. Spacecr. Rockets*, vol. 53, no. 2, pp. 241–248, 2016.
[16] K. T. Wilson and M. A. Peck, "Electromagnetic actuation for non-contact, propellant-free, six-degree-of-freedom relative mobility," in *Proc. AIAA Scitech Forum*, Jan. 2021, Art. no. 0074.

[17] R. Volpe and C. Circi, "Optical-aided, autonomous and optimal space rendezvous with a noncooperative target," *Acta Astronaut.*, vol. 157, pp. 528–540, 2019.
[18] C.-T. Chen, *Linear System Theory and Design*, 4th ed. Oxford, U.K.: Oxford Univ. Press, 2012.
[19] A. J. Petruska and J. J. Abbott, "Omnimagnet: An omnidirectional electromagnet for controlled dipole-field generation," *IEEE Trans. Magn.*, vol. 50, no. 7, Jul. 2014, Art. no. 8400810.
[20] A. J. Petruska, J. B. Brink, and J. J. Abbott, "First demonstration of a modular and reconfigurable magnetic-manipulation system," in *Proc. IEEE Int. Conf. Robot. Automat.*, 2015, pp. 149–155.
[21] A. J. Petruska and J. J. Abbott, "Optimal permanent-magnet geometries for dipole field approximation," *IEEE Trans. Magn.*, vol. 49, no. 2, pp. 811–819, Feb. 2013.

Devin K. Dalton (Member, IEEE) received the B.S. degree in mechanical engineering with a minor in Portuguese from Utah State University, Logan, UT, USA, in 2009, the M.S. degree in aeronautical engineering from the Air Force Institute of Technology, Dayton, OH, USA, in 2014, and the Ph.D. degree in mechanical engineering (robotics track) from the University of Utah, Salt Lake City, UT, in 2023.

He is currently a Lt. Col. with the United States Air Force, Albuquerque, NM, USA, and the Chief of the Engineering Liaison Office, Ramstein AB, Germany.

Griffin F. Tabor (Member, IEEE) received the B.S. degree in robotics engineering from Worcester Polytechnic Institute, Worcester, MA, USA, in 2018. He is currently pursuing the Ph.D. degree in computing (robotics track) from the University of Utah, Salt Lake City, UT, USA, under the guidance of Dr. Tucker Hermans.

Tucker Hermans (Senior Member, IEEE) received the A.B. degree in German and computer science from Bowdoin College, Brunswick, ME, USA, in 2009, and the M.Sc. degree in computer science and the Ph.D. degree in robotics from Georgia Tech, Atlanta, GA, USA, in 2012 and 2014, respectively.

He was a Postdoc with TU Darmstadt, Darmstadt, Germany. He is currently an Associate Professor with the Kahlert School of Computing, University of Utah, Salt Lake City, UT, USA, and a Senior Research Scientist with NVIDIA, Santa Clara, CA, USA.

Dr. Hermans is a Founding Member of the University of Utah Robotics Center. He was the recipient of the NSF CAREER award, the 3 M Non-Tenured Faculty Award, and the Sloan Fellowship. His research has won multiple conference paper awards including winning the Best Medical Robotics Paper at ICRA 2017 and the Best Systems Paper at CoRL 2019.

Jake J. Abbott (Senior Member, IEEE) received the B.S. degree from Utah State University, Logan, UT, USA, in 1999, the M.S. degree from the University of Utah, Salt Lake City, UT, USA, in 2001, and the Ph.D. degree from Johns Hopkins University, Baltimore, MD, USA, in 2006, all in mechanical engineering.

In 2006, he was a Postdoctoral Researcher with ETH Zurich, Zurich, Switzerland. In 2008, he joined the Department of Mechanical Engineering, University of Utah, where he is currently a Professor. He is also currently the Director of the University of Utah Robotics Center.

Dr. Abbott's research has won multiple conference paper awards including the Best Manipulation Paper at ICRA 2010, the Best Paper at Haptics Symposium 2014, and the Best Medical Robotics Paper at ICRA 2017. He was awarded the Distinguished Service Award: Outstanding Reviewer for the Period 2015-2019 by IEEE Robotics and Automation Letters.